CAMES, **29**(1–2): 7–31, 2022, doi: 10.24423/cames.372

This article belongs to the *Special Issue on Advanced Optimization Methods for Uncertainties in Intelligent Industrial Systems* edited by Dr. I.J. Jacob, Dr. B.H. bin Ahmad and Dr. Z.F. Khan

Automated Lung Nodule Detection in CT Images by Optimized CNN: Impact of Improved Whale Optimization Algorithm

M. Kiran KUMAR, Anthoniraj AMALANATHAN*

School of Computer Science & Engineering
Vellore Institute of Technology
Vellore, Tamilnadu, India
*Corresponding Author e-mail: aanthoniraj@vit.ac.in

Lung cancer is one of the leading causes of cancer-related deaths among individuals. It should be diagnosed at the early stages, otherwise it may lead to fatality due to its malicious nature. Early detection of the disease is very significant for patients' survival, and it is a challenging issue. Therefore, a new model including the following stages: (1) image pre-processing, (2) segmentation, (3) proposed feature extraction and (4) classification is proposed. Initially, pre-processing takes place, where the input image undergoes specific pre-processing. The pre-processed images are then subjected to segmentation, which is carried out using the Otsu thresholding model. The third phase is feature extraction, where the major contribution is obtained. Specifically, 4D global local binary pattern (LBP) features are extracted. After their extracting, the features are subjected to classification, where the optimized convolutional neural network (CNN) model is exploited. For a more precise detection of a lung nodule, the filter size of a convolution layer, hidden unit in the fully connected layer and the activation function in CNN are tuned optimally by an improved whale optimization algorithm (WOA) called the whale with tri-level enhanced encircling behavior (WTEEB) model.

Keywords: lung disease, pre-processing, segmentation, feature extraction, classification, performance.

Notation

ANN – artificial neural network,
AUC – area under the curve,
CAD – computer-aided detection,
CNN – convolutional neural network,
CT – computed tomography,
CXR – chest X-ray,
DeepLN – deep neural network-based lung nodule detection system,
FDR – false discovery rate,
FMS – F-measure,

FNR – false negative rate,
FPR – false positive rate,
GLCM – gray-level co-occurrence matrix,
GGO – ground glass opacity,
LBP – local binary pattern,
MCC – Matthews correlation coefficient,
NN – neural network,
NPV – net predictive value,
PNN – probabilistic neural network,
SVM – supply vector machine,
WOA – whale optimization algorithm,
WTEEB – whale with tri-level enhanced encircling behavior.

1. Introduction

Cancer [9, 10] is one of the most deadly diseases studied in the present. In 2016, about 8.9 million people were reported to die because of the various effects of cancer. In the world, every sixth death is cancer-related, which makes it the second cause of death. Furthermore, lung cancer is among the most deadly diseases [11–14]. The main reason for lung cancer is the formation of cancerous nodules in the lobes of the lung. Yet, still as of now, no symptoms are defined using pulmonary nodules. Most of them are identified for reasons other than pulmonary nodules using a CXR. Hence, it is important to detect the nodules early as well for correct treatment. In computed tomographic images, nodules are the small dots, and therefore the clinicians have to inspect every image individually. This is time-consuming and may lead to ignoring or overlooking the features of the nodule.

The most powerful technique to detect lung cancer in the early stage is low-dose CT detecting the malignant primary lung nodules [15–18]. The radiologists' careful examination of these lung nodules in every CT image is a very tiring task because of their large number. In addition, the radiologists' knowledge and experience plays a key role in the diagnosis of the lung nodule. Due to various levels of knowledge and experience, a diagnosis or failure to make a diagnosis is likely to occur. In order to minimize these drawbacks, computer-aided detection (CAD) is deployed, which can predict the possibility of cancer and determine the lung nodules' location. CAD greatly assists radiologists in the quick and accurate detection of lung cancer.

The core functions in CAD systems are: pathological analysis, lesion detection, lesion body segmentation using machine learning algorithms [21, 22, 24, 25], and image processing techniques. These CAD structures greatly improve detection and diagnosis efficiency, and rectify some possible errors.

In the literature, the extraction of invariant features was conducted and presented to differentiate between false and real nodules based on ANNs and genetic

algorithms during the process of classification. Lung nodules are classified into two categories: malignant and benign. Nevertheless, the classification of lung nodules presents a challenge because of their diverse scales, densities, and shapes, making them hard to be generalized into a particular category. These differences in nodules maximize the difficulty in lung nodules detection, and therefore some potential CAD [19, 20, 23] schemes are needed for attaining more satisfactory detection performance.

The major contributions of this work are as follows:

- Pre-processed images are segmented using the Otsu thresholding model and the features such as 4D global LBP features are extracted along with conventional gray-level co-occurrence matrix (GLCM) features and other features.
- A new improved WOA algorithm is introduced, which is the enhanced version of the traditional WOA model.
- The advantage of the proposed work is evaluated and compared with existing classifiers with respect to different measures.

This paper is organized as follows: Section 2 presents various detection approaches for lung cancer nodules. Section 3 describes a novel lung nodule detection model and its overall framework, and Sec. 4 presents the description towards the proposed feature extraction and classification phase. In addition, Sec. 5 introduces the improved WOA, including its objective and solution encoding. Section 6 discusses the outcomes and the work is concluded by Sec. 7.

2. Literature survey

2.1. Related works

In 2019, Li *et al.* [1] introduced the lung nodule detection approach based on the deep learning model. The features were extracted by deploying patch-based multi-resolution convolutional networks and facilitated four diverse fusion models for classification. The simulation experiment on the proposed approach showed effective performance and superior robustness compared to other existing conventional models. The analysis showed that the introduced technique attained enhanced R-CPM and FAUC and was applicable for clinical practices.

In 2020, Kuo *et al.* [2] introduced an image processing technique to detect solid nodules, part solid and GGO within computed tomography of the chest. The main processes involved were lung segmentation, candidate detection, nodule enhancement, reduction of false positives and image preprocessing. The computing-intensive iterative hole-filling model was deployed for lung segmentation. Image accumulation was employed to extract the nodules, and the SVM was applied to reduce the positives. The outcome of the experiment showed that the im-

plemented rapid detection structure attained the least false positives and large sensitivity.

In 2019, Xu *et al.* [3] constructed the DeepLN dataset, which was the multi-resolution CT screening image dataset. The efficiency and correctness of lung nodule annotation were guaranteed by introducing a semi-automatic annotation system and a three-level labeling criterion. Furthermore, a new model named DeepLN was introduced to detect lung nodules in CT images. The lung nodules were located by extracting the multi-level features using NN-based detector. The simulation analysis produced a better recognition of nodules by the proposed method.

In 2018, Gu *et al.* [4] suggested a CAD structure for detecting lung nodules by deploying a 3D deep CNN merged with a multi-scale prediction scenario. This method has assisted the radiologists by offering precise detection of lung nodules. After the segmentation process, the lung nodules were detected by applying a 3D deep CNN with a multi-scale prediction. The proposed model attained more discriminative features. In addition, a multi-scale lung nodule prediction strategy that included multi-scale cube clustering and cube prediction was used for detecting extremely small nodules.

In 2019, Wang *et al.* [5] implemented a novel CAD scheme by means of CNNs and segmentation approaches for studying the problems in lung nodule detection. The system complexity was reduced by setting patches of CT images inside CNNs. In particular, every CT image was split into diverse patches, partitioned into six kinds, including three non-nodule kinds and three nodule kinds. The comparative analysis was made against the diverse CNNs architectures and revealed the superiority of the proposed work with larger number of false positives and high detection sensitivity.

In 2018, Wozniak *et al.* [6] presented a novel classification model for lung carcinomas. For every original image's pixel, this approach begins with the extraction and localization of lung nodules by evaluating the local variance. The local maxima were determined in the variance image. The contours of the feasible nodules in lung tissues were determined by using these maxima locations in the original image. However, after the segmentation process, many false nodules could be detected. Hence, a probabilistic neural network was used as the classifier for discriminating against the true nodules.

In 2019, Zuo *et al.* [7] suggested a multi-resolution CNN for extracting the features of diverse resolutions and levels from various network depth layers for lung nodule candidate classification. The model was partitioned into three phases via the use of knowledge transfer. Initially, the knowledge was transferred from the source CNN approach that was adapted to edge recognition and enhanced the method as a novel approach. Therefore, the method is applicable for the task of image classification. This implemented model's simulation achieved improved precision, accuracy and AUC compared to the other conventional models.

In 2018, Jiang *et al.* [8] established an efficient module for recognizing nodules based on multi-group patches of lung images. An efficient detection approach was proposed based on lung image patterns and was improved by the Frangi filter. The four-channel CNN method was modeled by merging the two image groups to study the radiologist's ability to detect the four-level nodules. The result thus experimented and achieved with better sensitivity and reduced false positives, and has explained the effective improvement in the detection performance of lung nodule.

2.2. Review

Table 1 presents merits and demerits of the discussed above conventional approaches in lung nodule detection. Various existing models are not well prepared to detect the lung nodules in the early stage. Hence, much attention is

Table 1. Reviews on conventional models in lung nodule detection.

Author	Methods	Features	Challenges
Li *et al.* [1]	CNN	• Achieves higher sensitivity • Accurate and robust to use in real-world applications	• Needs the optimization concept in CNN for further efficiency
Kuo *et al.* [2]	SVM	• Enhanced computation time • Improved detection rate	• Choosing appropriate kernel function is tricky
Xu *et al.* [3]	Deep LN	• Increases the effectiveness of the training process • Better prediction performance	• Robustness needs to be enhanced with more attention • The future task is on evaluating the lung nodules' malignancy grades
Gu *et al.* [4]	Deep CNN	• Superior detection of small lung nodules • Improved sensitivity	• Future work is on FP reduction • Needs further automatic classification of lung nodules
Wang *et al.* [5]	CNN	• The complexity of the system is reduced • Suitable to radiologists for diagnosis	• Detection sensitivity is not satisfactory • More CNNs with larger training sets are needed
Wozniak *et al.* [6]	PNN	• Clear classification rate • The capability of detecting low-contrast nodules	• Slower than multilayer perceptron network • Needs mode memory space
Zuo *et al.* [7]	CNN	• Better performance on classification • Improves the accuracy efficiently	• High computational cost • Needs a lot of training data
Jiang *et al.* [8]	CNN	• Reduces the false positives extremely • Improved detection precision	• Needs some expert knowledge • Comparatively slow

needed to improve the detection process. CNN is the methodology in [1] that achieves higher sensitivity and is more accurate and robust to use in real-world applications. However, the optimization concept in CNN needs further efficiency. SVM [2] has enhanced computation time and improved detection rate, but choosing an appropriate kernel function is tricky. Deep LN [3] increases the effectiveness of the training process and has better prediction performance. The main drawback of this model is its robustness, which needs to be enhanced with more attention and the future task is to evaluate the lung nodules' malignancy grades. Deep CNN [4] shows the superior detection of small lung nodules with improved sensitivity. The future work is mainly to reduce FPs. In addition, it needs automatic classification of lung nodules. CNN [5] proposes reduced system complexity and is suitable to radiologists for diagnosis. However, the detection sensitivity is not satisfactory and more CNNs with larger training sets are needed. PNN [6] has a clear classification rate with the capability of detecting low-contrast nodules. Still, it is slower than a multilayer perceptron network and needs mode memory space. CNN [7] poses better performance on classification and improves accuracy. Nevertheless, the computational cost is high and a lot of training data is needed.

3. A novel lung nodule detection model: Overall framework

Figure 1 depicts the architecture of the adopted lung nodule recognition model. The steps involved in this proposed model are: (1) image pre-processing, (2) segmentation, (3) proposed feature extraction and (3) classification. In the initial pre-processing phase, the input image undergoes certain processes such as read image, resizing, noise removal and morphology (smoothing edges). Subsequently, the segmentation of this pre-processed image is done using the Otsu thresholding technique. Feature extraction is the subsequent phase, where the major contribution is conducted. Particularly, the proposed 4D global LBP features are extracted along with conventional GLCM features and other features such as area and perimeter, long and short axis, etc.

After extracting these features, they are subjected to classification, where the optimized CNN model is used. As the proposed work contributes to the precise detection of a lung nodule, the filter size of a convolutional layer, hidden unit in the fully connected layer, and the activation function in CNN are optimally tuned by a WTEEB algorithm that is the enhanced version of WOA.

3.1. The Otsu thresholding-based segmentation

Once the pre-processing is completed, the pre-processed image undergoes the segmentation process via the Otsu thresholding [27]. In this process, the image

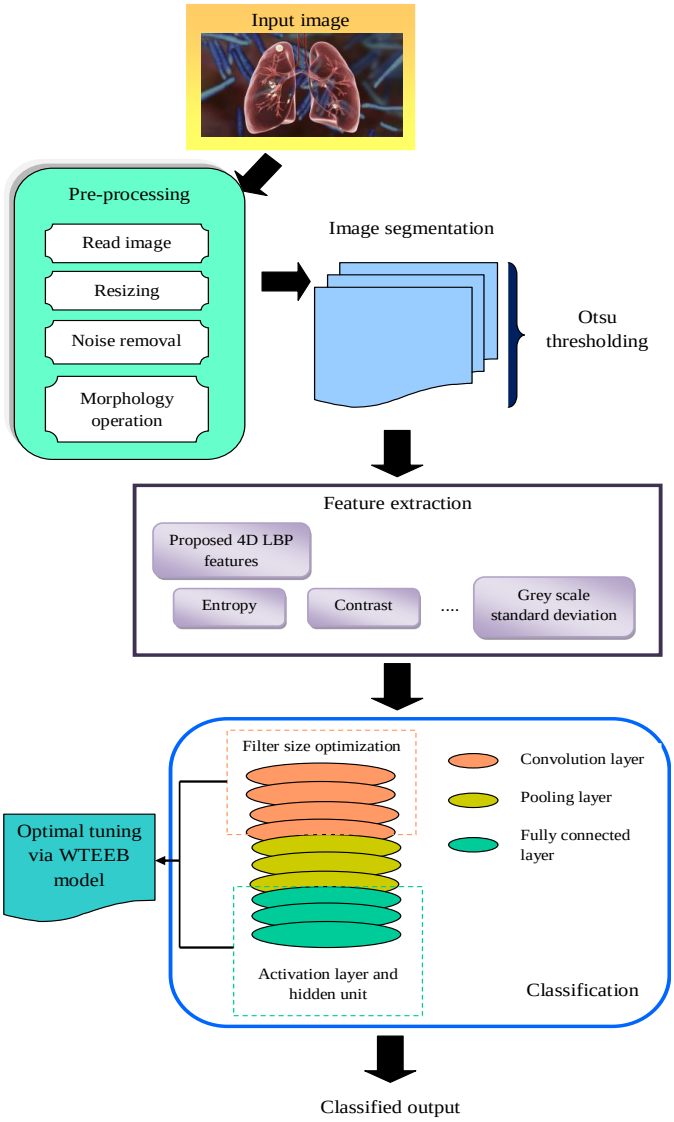

FIG. 1. The architecture of the proposed lung nodule detection model.

consists of an object and a background. The threshold value is fixed by the Otsu technique, and thus the overlap is decreased. Accordingly, the image is segmented into dark and light regions T_1 and T_0, and the level of intensity is represented in notation sequence $T_0 = (0, 1, ..., th\}$, and for the area $T_1 = (th, th+1, ..., \bar{l}-1, \bar{l}\}$, where the threshold is exhibited by th and the image maximum gray level is explicated by 1. The object and background are adopted with T_0 and T_1 or *vice versa*. This Otsu thresholding process is as follows:

Assume the histogram probability for gray value as $hp(\bar{i})$, $\bar{i} = 1, ..., \bar{l}$ and stated as:

$$hp(\bar{i}) = \frac{\text{no}\{(\overline{r}, \overline{c}) \,|\text{image}(\overline{r}, \overline{c}) = \bar{i}\}}{\overline{R} \cdot \overline{C}}. \tag{1}$$

The index images for column and row are expressed as $\overline{c}$ and $\overline{r}$, and their counts are expressed by $\overline{C}$ and $\overline{R}$.

The variance, mean and weight of class T_0 with intensity value from 0 to th are denoted by $\sigma_{\bar{b}}(th)$, $\mu_{\bar{b}}(th)$ and $\omega_{\bar{b}}(th)$, respectively. If their intensity falls between $th + 1$ and 1, they are represented as $\omega_{\bar{f}}(th)$, $\mu_{\bar{f}}(th)$ and $\sigma_{\bar{f}}(th)$. The weighted sum of cluster variances is referred as σ^2_{ω}.

The value with minimal class difference is assumed to be the optimal threshold value th^*. Equation (2) delineates the within-class variance:

$$\sigma^2_{\omega} = \omega_{\bar{b}}(th) \cdot \sigma^2_{\bar{b}}(th) + \omega_{\bar{f}}(th) \cdot \sigma^2_{\bar{f}}(th), \tag{2}$$

where

$$\omega_{\bar{b}}(th) = \sum_{\bar{i}=1}^{th} hp(\bar{i}), \tag{3}$$

$$\omega_{\bar{f}}(th) = \sum_{\bar{i}=th+1}^{\bar{l}} hp(\bar{i}), \tag{4}$$

$$\mu_{\bar{b}}(th) = \frac{\sum_{\bar{i}=1}^{th} \bar{i} \cdot hp(\bar{i})}{\omega_{\bar{b}}(th)}, \tag{5}$$

$$\mu_{\bar{f}}(th) = \frac{\sum_{\bar{i}=th+1}^{\bar{l}} \bar{i} \cdot hp(\bar{i})}{\omega_{\bar{f}}(th)}, \tag{6}$$

$$\sigma^2_{\bar{b}}(th) = \frac{\sum_{\bar{i}=1}^{th} (\bar{i} - \mu_{\bar{b}}(th))^2 \cdot hp(\bar{i})}{\omega_{\bar{b}}(th)}, \tag{7}$$

$$\sigma^2_{\bar{f}}(th) = \frac{\sum_{\bar{i}=th+1}^{\bar{l}} (\bar{i} - \mu_{\bar{f}}(th))^2 \cdot hp(\bar{i})}{\omega_{\bar{f}}(th)}. \tag{8}$$

4. Description towards proposed feature extraction and classification phase

4.1. The proposed 4D-global LBP features

The main contribution of this paper is the proposed feature extraction phase, in which the LBP feature is extracted based on the distance modality. Each region is comprised of eight neighborhood values n_0, n_1, n_2, n_3, n_4, n_5, n_6 and n_7 as $(x_{\min}, y_{\min})$, $(x_{\min}, y_{\text{center}})$, $(x_{\min}, y_{\max})$, $(x_{\text{center}}, y_{\max})$, $(x_{\max}, y_{\max})$, $(x_{\max}, y_{\text{center}})$, $(x_{\max}, y_{\min})$ and $(x_{\text{center}}, y_{\min})$, respectively. Based on these neighborhood values, the mean, median, min, and max values of LBP features are evaluated. The mean measure is calculated using Eq. (9):

$$D_1 = I_{\text{mean}}(\text{ROI}) = \sum_{\text{i}=0}^{7} \text{S}(\text{n}_\text{i} - \text{I}_\text{u})^{2^\text{i}}, \tag{9}$$

where I_u is the mean of all ROI pixels, and $S(n_i - I_u)$ is evaluated as per the conditions given in Eq. (10):

$$S(n_i - I_u) = \begin{cases} 1 & \text{if} \quad (n_i - I_u) \geq 0, \\ 0 & \text{otherwise.} \end{cases} \tag{10}$$

Similarly, the median, min and max values are evaluated as $D_2 = I_{\text{median}}(\text{ROI})$, $D_3 = I_{\min}(\text{ROI})$ and $D_4 = I_{\max}(\text{ROI})$, respectively. Similarly, these four values are evaluated for all existing regions in the lung nodules. Along with these proposed features, the conventional GLCM features such as contrast, energy, homogeneity, correlation, and ASM are also extracted. Furthermore, four other features such as area and perimeter, long and short axis, average gray-scale value and gray-scale standard deviation features are also extracted.

4.1.1. Contrast [28]. It is measured by the summation of diversity in the image's gray level. Equation (11) provides the calculation of the contrast value:

$$\text{Contrast} = \sum_{\widehat{p},\widehat{q}=0}^{\overline{N}-1} MA_{\widehat{p},\widehat{q}}(\widehat{p} - \widehat{q})^2. \tag{11}$$

4.1.2. Energy [28]. This is the measure to analyze the intensity in GLCM's gray level concentration. This, in turn, returns the summation of squared elements in GLCM. It is computed as:

$$\text{Energy} = \sqrt{\sum_{\widehat{p},\widehat{q}=0}^{\overline{N}-1} MA^2_{\widehat{p},\widehat{q}}}. \tag{12}$$

4.1.3. Homogeneity [28]. The inverse difference moment is the distribution of proximity measure within the elements over GLCM diagonal from GLCM. Homogeneity is calculated as:

$$\text{Homogeneity} = \sum_{\widehat{p},\widehat{q}=0}^{\overline{N}-1} \frac{MA_{\widehat{p},\widehat{q}}}{1+(\widehat{p}-\widehat{q})^2}. \tag{13}$$

4.1.4. Correlation [28]. An index, in which the reference pixel is correlated with the pixel along the distance and direction of the whole image, is given as pixel correlation. The calculation of this correlation value is shown in Eq. (14), and the mean and variance are determined in Eqs (15) and (16), respectively:

$$\text{Correlation} = \sum_{\widehat{p},\widehat{q}=1}^{\overline{N}} \frac{(\widehat{p}-\mu_{\widehat{p}})(\widehat{q}-\mu_{\widehat{q}})}{\sigma_{\widehat{p}}\sigma_{\widehat{q}}} MA_{\widehat{p},\widehat{q}}, \tag{14}$$

$$\mu_{\widehat{p}} = \sum_{\widehat{p}=1}^{\overline{m}} \widehat{p} \sum_{\widehat{q}=1}^{\overline{m}} MA_{\widehat{p},\widehat{q}}, \qquad \mu_{\widehat{q}} = \sum_{\widehat{q}=1}^{\overline{m}} \widehat{q} \sum_{\widehat{p}=1}^{\overline{m}} MA_{\widehat{p},\widehat{q}}, \tag{15}$$

$$\sigma_{\widehat{p}} = \sum_{\widehat{p}=1}^{\overline{m}} (\widehat{p}-\mu_{\widehat{p}})^2 \sum_{\widehat{q}=1}^{\overline{m}} MA_{\widehat{p},\widehat{q}}, \qquad \sigma_{\widehat{q}} = \sum_{\widehat{q}=1}^{\overline{m}} (\widehat{q}-\mu_{\widehat{q}})^2 \sum_{\widehat{p}=1}^{\overline{m}} MA_{\widehat{p},\widehat{q}}, \tag{16}$$

where the horizontal and vertical coordinate matrix is $\widehat{p}$ and $\widehat{q}$, respectively, and its matrix value is $MA_{\widehat{p},\widehat{q}}$.

4.1.5. Angular second moment [29]. It is the measurement of homogeneity and is estimated using Eq. (17):

$$\text{ASM} = \sum_{\widehat{p},\widehat{q}=0}^{\overline{N}-1} \left\{MA_{\widehat{p},\widehat{q}}\right\}^2. \tag{17}$$

4.1.6. Dissimilarity [29]. Dissimilarity measure is defined as the mean of the gray level difference distribution of the image. This is stated in Eq. (18):

$$\text{Dissimilarity} = \sum_{\widehat{p},\widehat{q}=0}^{\overline{N}-1} \left\{MA_{\widehat{p},\widehat{q}}\,|\widehat{p}-\widehat{q}|\right\}. \tag{18}$$

4.1.7. Perimeter and area [2]. The ratio of perimeter and area is calculated as shown in (19), where A is the block area or pixels count, and *Len* is defined as the count of pixels needed for surrounding the block:

$$\text{Ratio} = \frac{A}{Len}. \tag{19}$$

4.1.8. Short axis and long axis [2]. The long and round objects are distinguished using this measure. The EC ratio is presented in Eq. (20), in which the object's short axis and long axis are defined as *Minor* and *Major*, respectively:

$$\text{EC} = \frac{Minor}{Major}. \tag{20}$$

4.1.9. Average gray-scale values [2]. Every object is included with its own gray-scale value, and the average gray-scale value is evaluated in the object block $i(x, y)$ and is stated in Eq. (21):

$$\text{Mean} = \frac{\sum\limits_{x,y \in A} i(x, y)}{A}. \tag{21}$$

4.1.10. Gray-scale standard deviation [2]. The calculation of this gray-scale standard deviation is defined as:

$$\text{STD} = \sqrt{\frac{i}{N} \sum_{i=1}^{N} (x_i - \text{Mean})^2}. \tag{22}$$

All these features are then subjected to classification, the final phase, where the classified output is obtained.

4.2. Classification using optimized CNN

After the extraction of features, the classification is exploited for classifying the image. This classification is made using CNN [30], and the process is as follows. Even though the computer vision assignments are adopted with the NNs, the prior knowledge incorporation within the network architecture is appropriate for superior generalization performance.

4.2.1. Layers. Different layers exist in CNN. Complex architectures are constructed by stacking multiple layers and deployed for classification using these layers.

Convolutional layer. Consider the convolutional layer as cl. Consequently, the feature maps $\overline{r}_1^{(cl-1)}$ from previous layers, each with a size $\overline{r}_2^{(cl-1)} \times \overline{r}_3^{(cl-1)}$, consist of the input of the layer cl. When $cl = 1$, the input is retained as cl comprised of one or more channels, by which the raw data are accepted as input in CNN. The layer cl has the output that involves $\overline{r}_1^{cl}$ feature maps of size $\overline{r}_2^{cl} \times \overline{r}_3^{cl}$. $\widehat{X}_i^{cl}$ denotes the i-th feature map in layer cl and is evaluated as:

$$\widehat{X}_i^{cl} = B_i^{(cl)} + \sum_{j=1}^{\overline{r}_1^{(cl-1)}} P_{i,j}^{(cl)} \cdot \widehat{X}_j^{(cl-1)}, \tag{23}$$

where the bias matrix is expressed as $B_i^{(cl)}$ and the filter of size $(2s_1^{cl}+1) \times (2s_2^{cl}+1)$ relating the j-th feature map in a layer $cl-1$ along with the feature map in the layer cl is denoted as $P_{i,j}^{(cl)}$. **This filter size is optimally tuned for better performance using the proposed WTEEB algorithm.** The border effects influence the $\overline{r}_2^{cl}$ and $\overline{r}_3^{cl}$ as mentioned before. The output feature map is given the size defined in Eq. (24):

$$\overline{r}_2^{cl} = \overline{r}_2^{(cl-1)} - 2s_1^{cl} \quad \text{and} \quad \overline{r}_3^{cl} = \overline{r}_3^{(cl-1)} - 2s_2^{cl}. \tag{24}$$

Frequently, the filters used to compute the fixed feature map $\widehat{X}_i^{cl}$ are similar, i.e., $P_{i,j}^{(cl)} = P_{i,k}^{(cl)}$ for $j \neq k$. Every feature map $\widehat{X}_i^{cl}$ in the layer cl includes $\overline{r}_2^{cl} \cdot \overline{r}_3^{cl}$ units arranged in the form of the two-dimensional array. The output computed per the unit at the position (g, h) is given in Eqs (25) and (26):

$$\left(\widehat{X}_i^{cl}\right)_{g,h} = \left(D_i^{(cl)}\right)_{g,h} + \sum_{j=1}^{\overline{r}_1^{(cl-1)}} \left(P_{i,j}^{(cl)} * \widehat{X}_j^{(cl-1)}\right)_{g,h}, \tag{25}$$

$$\left(\widehat{X}_i^{cl}\right)_{g,h} = \left(D_i^{(cl)}\right)_{g,h} + \sum_{j=1}^{\overline{r}_1^{(cl-1)}} \sum_{d=-s_1^{cl}}^{s_1^{cl}} \sum_{e=-s_2^{cl}}^{s_2^{cl}} \left(P_{i,j}^{(cl)}\right)_{d,e} \left(\widehat{X}_j^{(cl-1)}\right)_{g+d,h+e}, \tag{26}$$

where $\widehat{X}_j^{(cl-1)}$ is the trainable weight of the network and bias matrix is given as $D_i^{(cl)}$. The skipping factors o_1^{cl} and o_2^{cl} can be determined by using the sub-sampling. The fundamental notation is to fix the count of pixels in the vertical and horizontal direction, once before applying the filter. The size of the output feature maps using the skipping factor is given as shown in Eq. (27):

$$\overline{r}_2^{cl} = \frac{\overline{r}_2^{(cl-1)} - 2s_1^{cl}}{o_1^{cl} + 1} \quad \text{and} \quad \overline{r}_3^{cl} = \frac{\overline{r}_3^{(cl-1)} - 2s_2^{cl}}{o_2^{cl} + 1}. \tag{27}$$

Non-linearity layer. Consider the layer cl as a non-linearity layer, where the input is $\overline{r}_1^{cl}$ feature maps, and the output is composed again with $\overline{r}_1^{cl} = \overline{r}_1^{(cl-1)}$ feature maps. Given the size of each as $\overline{r}_2^{(cl-1)} \times \overline{r}_3^{(cl-1)}$, this is denoted using Eq. (28):

$$\widehat{X}_i^{cl} = f(\widehat{X}_i^{(cl-1)}), \tag{28}$$

where the activation function used in the layer cl is given as σ and operates pointwise. The additional gain coefficient is given using the following Eq. (29):

$$\widehat{X}_i^{cl} = ga_i f(\widehat{X}_i^{(cl-1)}). \tag{29}$$

Rectification. Consider the rectification layer as cl. The absolute value for every component of the feature maps is computed as in Eq. (30) and the input consists of the $\overline{r}_1^{(cl-1)}$ feature map of size $\overline{r}_2^{(cl-1)} \times \overline{r}_3^{(cl-1)}$

$$\widehat{X}_i^{cl} = \left|\widehat{X}_i^{cl}\right|, \tag{30}$$

where the absolute value is evaluated pointwise so that the output includes the $\overline{r}_1^{cl} = \overline{r}_1^{(cl-1)}$ feature maps not modified in size.

Local contrast normalization layer. Take the contrast normalization layer cl. The main aim of the layer is to impose native aggressiveness amongst the adjacent units inside the feature maps and units within the similar abstraction location in varied feature maps. The afforded feature maps of size $\overline{r}_2^{(cl-1)} \times \overline{r}_3^{(cl-1)}$ as $\overline{r}_1^{(cl-1)}$ the $\overline{r}_1^{cl} = \overline{r}_1^{(cl-1)}$ since the feature maps are included in the output layer cl with no adjustment in size. Equation (1) is used to calculate the subtractive normalization procedure (31). The layer's output cl is given in Eq. (32), where K and μ are the hyper-parameters [31]:

$$(\widehat{X}_i^{cl})_{g,h} = \widehat{X}_i^{(cl-1)} - \sum_{j=1}^{\overline{r}^{(cl-1)}} P_{F(\sigma)} * \widehat{X}_j^{(cl-1)}, \tag{31}$$

$$(\widehat{X}_i^{cl})_{g,h} = \frac{(\widehat{X}_i^{(cl-1)})_{g,h}}{\left(K + \mu \sum\limits_{j=1}^{\overline{r}_1^{cl-1}} (\widehat{X}_i^{(cl-1)})_{g,h}^2\right)^{\mu}}. \tag{32}$$

Feature pooling and subsampling layer. Consider cl as the pooling layer and their outputs $\overline{r}_1^{cl} = \overline{r}_1^{(cl-1)}$ feature maps of the smallest possible size. In general, the pooling formula in every feature map is formed by placing the windows at over-lapping points and maintaining one value for each window, resulting in feature map subsampling.

Fully connected layer. Consider a fully connected layer as cl. If the layer $cl-1$ is not fully linked, then the layer cl accepts input other than $\overline{r}_1^{(cl-1)}$ feature maps of size $\overline{r}_2^{(cl-1)} \times \overline{r}_3^{(cl-1)}$ and the j layer with i-th unit is evaluated in Eq. (33). Here, the hidden unit hi of this fully connected layer is optimally tuned by the proposed WTEEB algorithm

$$\widehat{x}_i^{cl} = f(v_i^{cl}) \quad \text{with} \quad v_i^{cl} = \sum_{j=1}^{\overline{r}_1^{cl-1}} \sum_{g=1}^{\overline{r}_2^{cl-1}} \sum_{h=1}^{\overline{r}_3^{cl-1}} W_{i,j,g,h}^{cl} \left(\widehat{X}_j^{(cl-1)} \right), \tag{33}$$

where the weight corresponding to the unit at the position (g, h) in the j-th feature map of layer $cl-1$ and the i-th unit in the layer cl is $W_{i,j,g,h}^{cl}$ [31]. The CNN process results in the classified output, and the optimized CNN model is presented in Fig. 2.

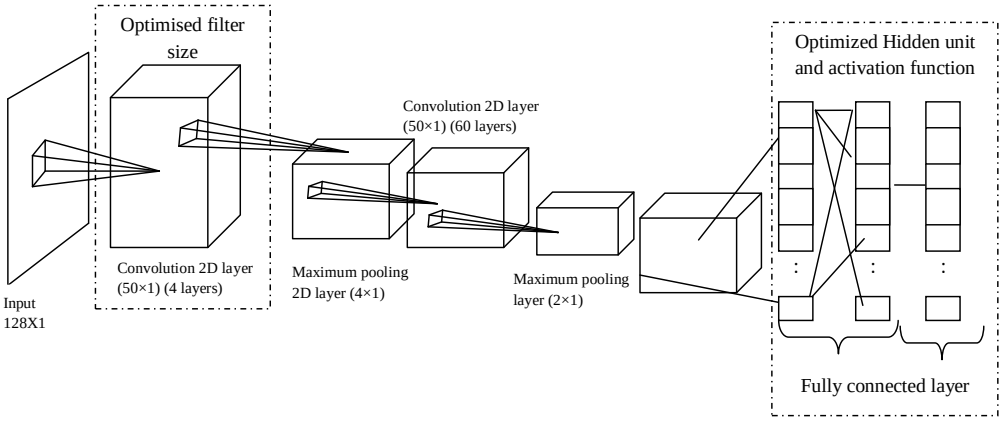

FIG. 2. The optimized CNN model.

5. Improved whale optimization algorithm: Objective and solution encoding

5.1. Solution encoding

As mentioned above, the optimization logic used in this work helps in the precise detection of the nodule. The activation function σ is particularly fine-tuned for selecting the appropriate functions such as sigmoid, softmax, linear, ReLu or tanh. Furthermore, the hidden unit (hi) and filter size of convolutional layers are also defined optimally. A new algorithm named WTEEB is introduced in this work to make this possible. The input solution to this proposed algorithm

is illustrated in Fig. 3. Furthermore, the objective function defined in this work is stated in Eq. (34), where *acc*is detection accuracy:

$$obj = \max(acc). \tag{34}$$

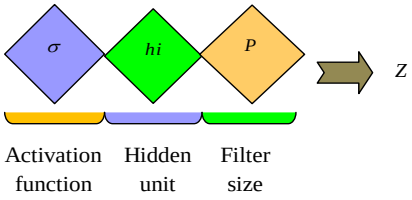

FIG. 3. Solution encoding.

5.2. The proposed WTEEB algorithm

The developed model is the enhanced version of WOA with an improved working principle. This improves the performance with respect to better convergence rate and speed. The mathematical representation of the proposed algorithm is explained below.

5.2.1. Updated shrinking encircling mechanism. At the beginning of the hunting process, the prey gets encircled by the whales and then updates their position to the optimum solution. A new evaluation for shrinking encircling is proposed, and it is defined in Eq. (35). In fact, the position vectors of the present search agent, under all the cases: best, worst and average, are considered with the proposed evaluation. In Eq. (35), the present iteration is t, vector coefficients are represented as $\mathbf{L}$ and $\mathbf{K}$, the position vector of the best solution is $\mathbf{Z}^*$, the position vector is $\mathbf{Z}$, value is portrayed as $||$ and the element-by-element multiplication is expressed as " $\cdot$ ". Similarly, the position of the worst solution is $\mathbf{Z}^{\text{worst}}$, and the average of the entire solution pool is $\mathbf{Z}^{\text{avg}}$ [32]:

$$\mathbf{G} = \frac{|\mathbf{K}_1 \cdot \mathbf{Z}^*(t) - \mathbf{Z}(t)| + \left|\mathbf{K}_2 \cdot \mathbf{Z}^{\text{worst}}(t) - \mathbf{Z}(t)\right| + |\mathbf{K}_3 \cdot \mathbf{Z}^{\text{avg}}(t) - \mathbf{Z}(t)|}{3}, \tag{35}$$

$$\mathbf{Z}(t+1) = \mathbf{Z}^*(t) - \mathbf{L} \cdot \mathbf{G}. \tag{36}$$

After determining the better solution, $\mathbf{Z}^*$, $\mathbf{Z}^{\text{worst}}$ and $\mathbf{Z}^{\text{avg}}$ need to be updated on each trail run. $\mathbf{L}$ and $\mathbf{K}$ are evaluated using Eqs (37) and (38). In this, the $\mathbf{q}$ value is sequentially reduced from 2 to 0, and the random vector $\mathbf{r}$ is restricted within $[0, 1]$

$$\mathbf{L} = 2\mathbf{q} \cdot \mathbf{r} - \mathbf{q}, \tag{37}$$

$$\mathbf{K}_i = 2\mathbf{r}_i, \qquad i = 1, 2, 3. \tag{38}$$

5.2.2. Spiral updating position. The spiral equation is arithmetically given for the position update among prey and humpback whale and is evaluated in Eqs (39) and (40). Here, the logarithmic spiral shape is explicated by b, and the uniform distribution of arbitrary integer l is in the range $[-1, 1]$. The probability of every encircling path is signified as pl in Eq. (41):

$$\mathbf{G}' = \left|\mathbf{Z}^*(t) - \mathbf{Z}(t)\right|, \tag{39}$$

$$\mathbf{Z}(t+1) = \mathbf{G}' \cdot e^{ad} \cdot (\cos 2\pi d) + \mathbf{Z}^*(t), \tag{40}$$

$$\begin{aligned} &\mathbf{Z}(t+1) = \mathbf{Z}^*(t) - \mathbf{L} \cdot \mathbf{G} \quad \text{if} \quad pl < 0.5, \\ &\mathbf{Z}(t+1) = \mathbf{G}' \cdot e^{ad} \cdot (\cos 2\pi d) + \mathbf{Z}^*(t) \quad \text{if} \quad pl \geq 0.5. \end{aligned} \tag{41}$$

The pseudo-code and the flowchart for the proposed WTEEB algorithm are illustrated in Algorithm 1 and Fig. 3, respectively:

$$\mathbf{G} = \left|\mathbf{K} \cdot \mathbf{Z}_{\text{rand}} - \mathbf{Z}(t)\right|, \tag{42}$$

$$\mathbf{Z}(t+1) = \mathbf{Z}_{\text{rand}} - \mathbf{L} \cdot \mathbf{G}. \tag{43}$$

Algorithm 1. Pseudo-code of the proposed WTEEB algorithm.

Initialize the whale population Z_i $(i = 1, 2, ..., n)$
Compute fitness
Z^* = optimal agent
While $(t < \max t)$
    For all search agents
        Update q, L, K, d and pl
        if $(pl < 0.5)$
            if $(|L| < 1)$
                Update the position via new evaluation in Eq. (35)
            Else if $(|L| \geq 1)$
                Select arbitrary search agent (Z_{rand})
                Update position by Eq. (43)
            End if
        Else if $(pl \geq 0.5)$
            Update position by Eq. (40)
        End if
    End for
    Confirm if any search agents left the search space
    Compute fitness
    Update Z^* based on the optimal solution
    $t = t + 1$
End while
return Z^*

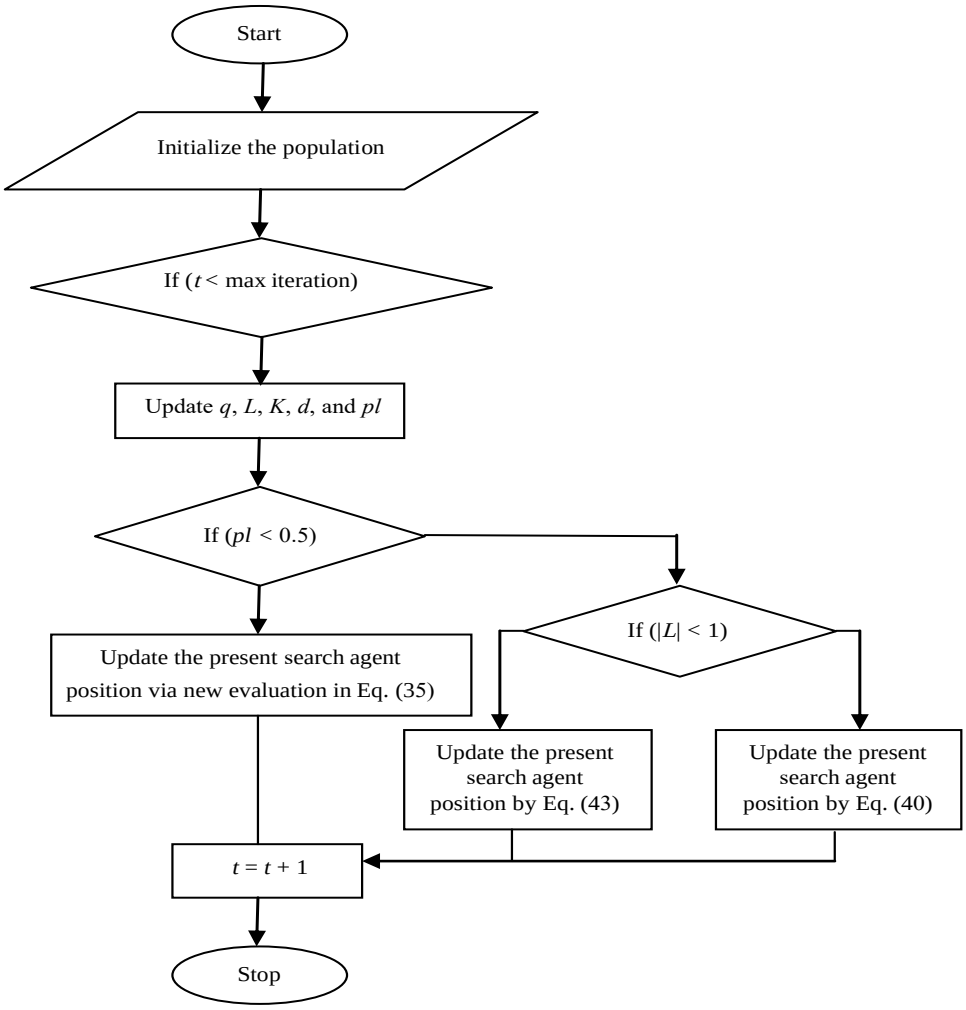

FIG. 4. The flowchart of the proposed WTEEB algorithm.

6. Results and discussions

6.1. Stimulation setup

The adopted lung nodule detection system using the WTEEB model was executed in Python. The dataset used for the implementation is the LIDC-IDRI dataset. The sample image representation is shown in Fig. 5. The improvement of the presented technique was distinguished over existing classifiers such as SVM+existing features [2], CNN+LBP, CNN [1], 4D-LBP+WOA-CNN models. Moreover, performance analysis was carried out with respect to measures such as accuracy, sensitivity, specificity, precision, FPR, FNR, FMS, NPV, MCC, and

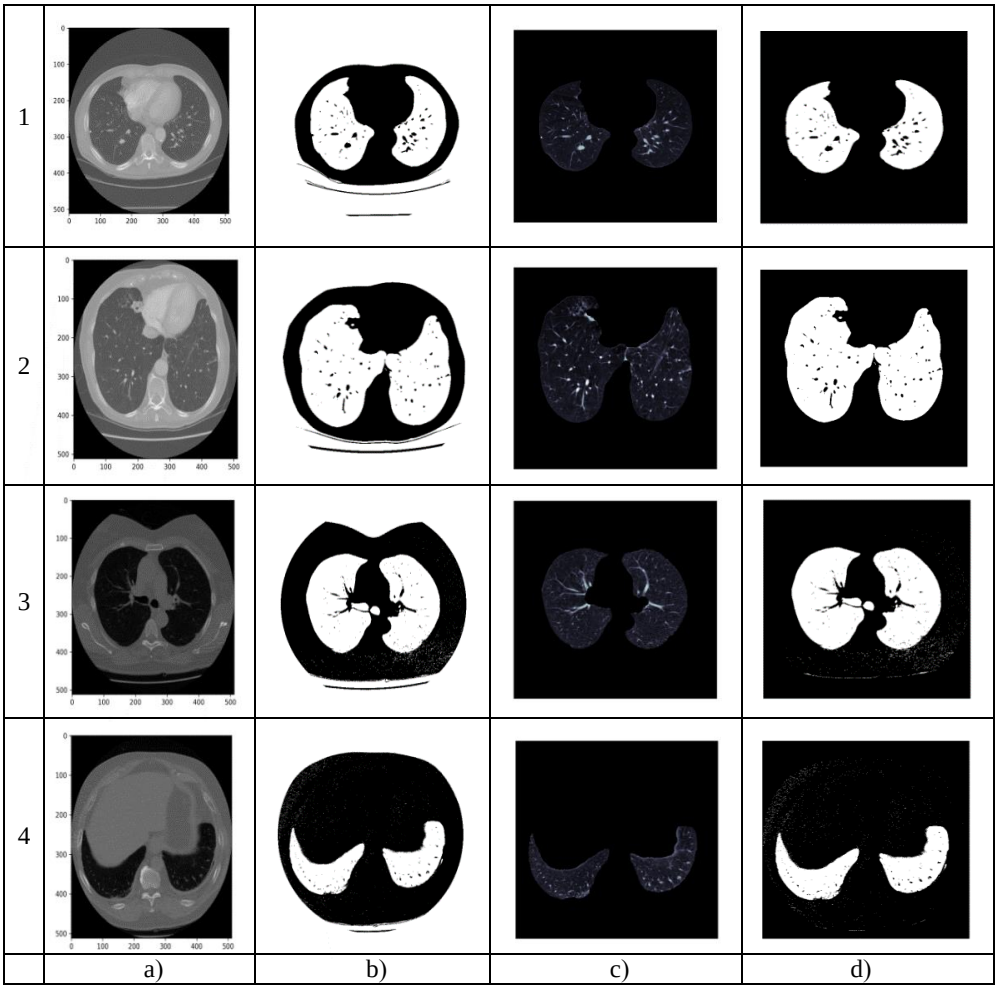

Fig. 5. Sample illustration of image results under the feature extraction (a) input, (b) binary, (c) bmask and (d) cleared.

FDR, respectively by varying the training percentages from 40, 50, 60, 70, 80 and 90. Moreover, statistical analysis was performed for describing the best, worst, mean and median performances of the adopted scheme over the other comparable schemes.

6.2. Performance analysis

The performance analysis of the presented approach compared with other conventional models by changing the training percentages from 40, 50, 60, 70, 80 and 90 is given in Figs 6 and 7. Figure 6 shows the positive measures, while

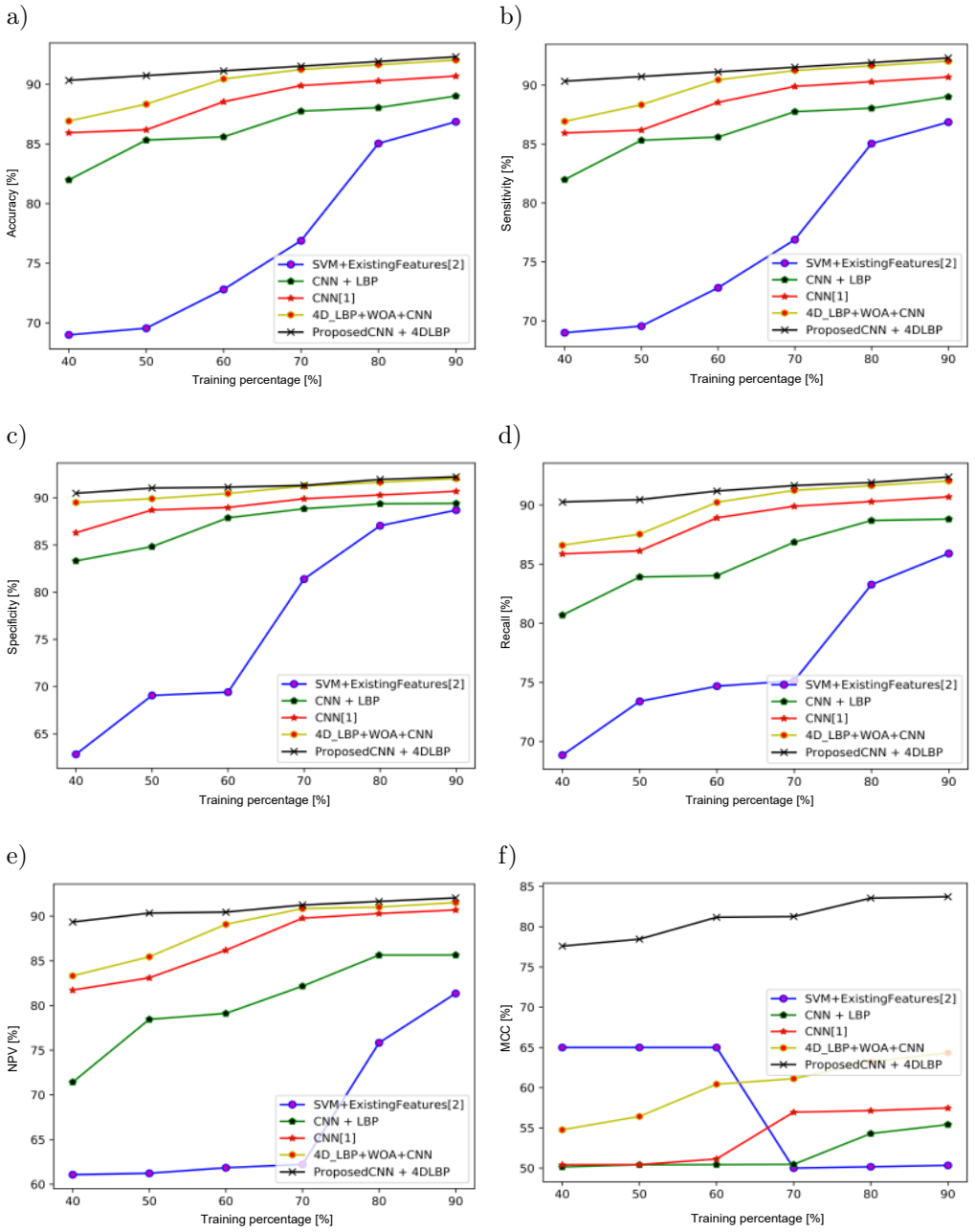

FIG. 6. Performance analysis of the proposed and conventional models concerning positive measures such as (a) accuracy, (b) sensitivity, (c) specificity, (d) recall, (e) NPV, (f) MCC.

Fig. 7 portrays the analysis of negative measures. Here, all the attained outcomes for the presented WTEEB model have achieved optimal values when

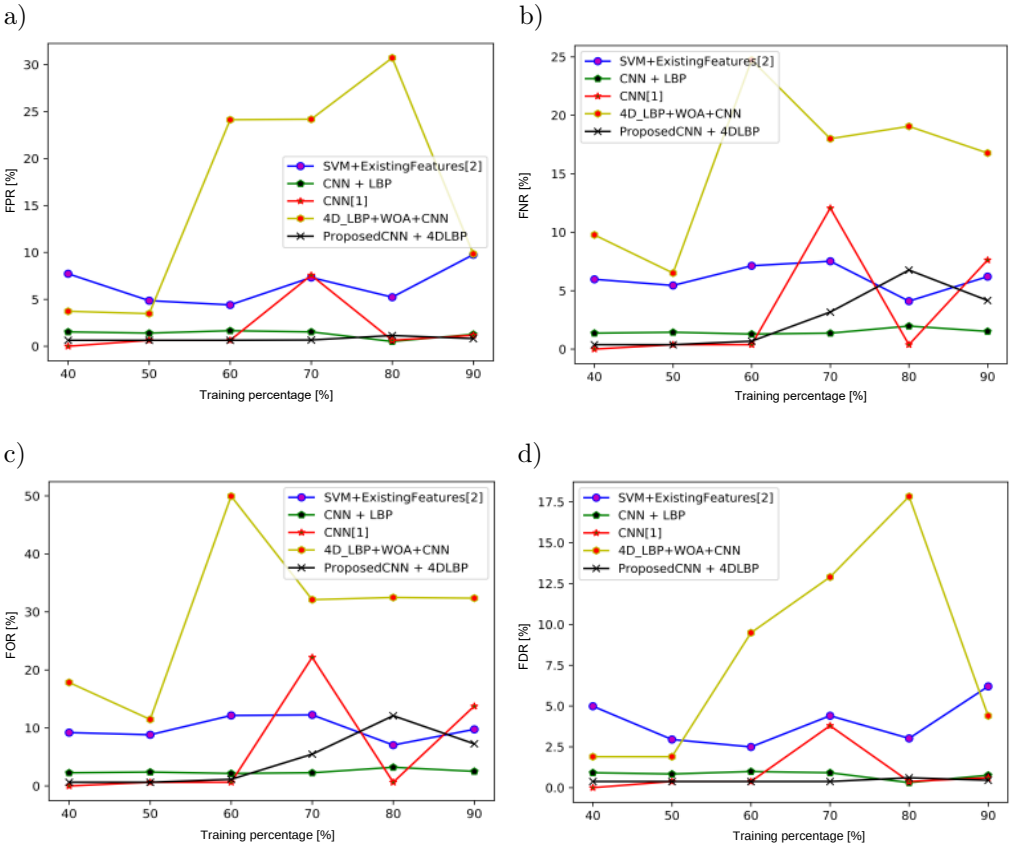

Fig. 7. Performance analysis of the proposed and conventional models concerning negative measures such as (a) FPR, (b) FNR, (c) FOR, (d) FDR.

evaluated over the other models. Especially, in Fig. 6a, the accuracy of the presented model at 90th training percentage is 5.9%, 3.57%, 1.76%, and 0.29% better than SVM+existing features, CNN+LBP, CNN, and 4D-LBP+WOA-CNN models. In Fig. 6b, the suggested scheme in terms of sensitivity is 23.23%, 7.78%, 5.03%, and 3.33% better than SVM+existing features, CNN+LBP, CNN and 4D-LBP+WOA-CNN models at 50th training percentage. In Fig. 6c, the specificity of the adopted scheme is 44%, 8.59%, 4.84%, and 1.09% better than SVM+existing features, CNN+LBP, CNN and 4D-LBP+WOA-CNN models at 40th training percentage. Moreover, in Fig. 6d, the recall of the implemented scheme at 90th training percentage is 7.52%, 4%, 1.85%, and 0.36% better than SVM+existing features, CNN+LBP, CNN, and 4D-LBP+WOA-CNN models. In addition, by examining the NPV metric in Fig. 6e we observe that the adopted scheme at 90th training percentage is 13.13%, 7.46%, 1.48%, and 0.57% better than SVM+existing features, CNN+LBP, CNN, and 4D-LBP+WOA-CNN

models. The analysis of the MCC in Fig. 6f shows that the adopted scheme is 66.29%, 51.11%, 45.69%, and 30.16% better than SVM+existing features, CNN+LBP, CNN, and 4D-LBP+WOA-CNN models. Also, in Fig. 7d, the FDR of the implemented scheme at 90th training percentage is 92.66%, 40.46%, 24.99%, and 89.66% better than SVM+existing features, CNN+LBP, CNN, and 4D-LBP+WOA-CNN models. Thus, the enhancement of the adopted WTEEB scheme has been verified from the analysis outcomes.

6.3. Statistical analysis

The statistical analysis of the adopted WTEEB algorithm in terms of accuracy is presented in Table 2. Usually, the meta-heuristic algorithms are stochastic in nature, and therefore, to attain precise results, the algorithm is executed five times and the outcomes are obtained. The adopted WTEEB model has attained optimal values for best, worst, mean and median values on the analysis outcomes. For example, the suggested scheme in terms of best performance is 5.9%, 3.57%, 1.76%, and 0.29% better than SVM+existing features, CNN+LBP, CNN, and 4D-LBP+WOA-CNN models. The mean performance of the implemented model in terms of accuracy is 19.08%, 5.84%, 3.09%, and 1.35% better than SVM+existing features, CNN+LBP, CNN, and 4D-LBP+WOA-CNN models. Also, the median performance of the adopted scheme is 22.02%, 5.37%, 2.37%, and 0.53% better than SVM+existing features, CNN+LBP, CNN, and 4D-LBP+WOA-CNN models. Thus, the betterment of the presented model has been confirmed from the outcomes.

Table 2. Statistical analysis in terms of accuracy: proposed *versus* conventional models.

Measures	SVM+existing features [2]	CNN+LBP	CNN [1]	4D-LBP+WOA-CNN	WTEEB
Best	86.85565	89.00973	90.68400	92.03040	92.30419
Worst	68.99062	81.98623	85.94271	86.91583	90.33272
Mean	76.69000	86.28000	88.58000	90.10000	91.32000
Median	74.84000	86.67000	89.21000	90.84000	91.32000

6.4. Overall performance analysis

Table 3 demonstrates the overall performance analysis of the adopted WTEEB model compared to the traditional methods. The analysis was carried out for each performance measure to validate the improvement of the presented scheme. More specifically, in Table 3, the adopted model in terms of accuracy is 19.02%, 4.29%, 1.81%, and 0.3% better than SVM+existing features, CNN+LBP, CNN, and 4D-LBP+WOA-CNN models. The adopted WTEEB model' sensitivity is

Table 3. Overall performance analysis of the implemented model over the traditional models.

Measures	SVM+existing features [2]	CNN+LBP	CNN [1]	4D-LBP+WOA-CNN	WTEEB
Accuracy	76.886110	87.744420	89.892000	91.23840	91.515610
Sensitivity	75.133950	86.852210	89.892000	91.23840	91.642520
Specificity	81.389950	88.836720	89.892000	91.23840	91.302520
Recall	75.133950	86.852210	89.892000	91.23840	91.642520
FPR	7.327586	1.528662	7.564297	24.18208	0.669344
FNR	7.518797	1.365706	12.066570	18.00000	3.171091
FMS	80.333900	88.966590	89.892000	91.23840	91.781790
NPV	62.215540	82.157760	89.758980	90.83965	91.238400
MCC	50.000000	50.467240	56.955510	61.11504	81.264620
FDR	4.404145	0.914634	3.793627	12.89833	0.379363

21.97%, 5.51%, 1.95%, and 0.44% better than SVM+existing features, CNN+LBP, CNN, and 4D-LBP+WOA-CNN models. The specificity of the adopted scheme is 12.18%, 2.78%, 1.57%, and 0.07% better than SVM+existing features, CNN+LBP, CNN, and 4D-LBP+WOA-CNN models. The recall in the adopted WTEEB model is 21.97%, 5.52%, 1.95%, and 0.44% better than SVM+existing features, CNN+LBP, CNN, and 4D-LBP+WOA-CNN models. Thus, the overall analysis proves the superiority of the adopted scheme.

7. Conclusion

This paper introduced a new lung cancer detection process, where the pre-processed images were segmented using the Otsu thresholding model. Then, the features such as 4D global LBP features were extracted along with the conventional GLCM features and other features. In addition, a new WTEEB model was introduced, which is the enhanced version of the traditional WOA model. Finally, analysis was conducted to validate the performance of the presented model. In the analysis, the accuracy of the presented model at 90th training percentage was 5.9%, 3.57%, 1.76% and 0.29% better than SVM+existing features, CNN+LBP, CNN and 4D-LBP+WOA-CNN models. Likewise, the suggested scheme in terms of sensitivity was 23.23%, 7.78%, 5.03% and 3.33% better than SVM+existing features, CNN+LBP, CNN and 4D-LBP+WOA-CNN models at 50th training percentage. The adopted scheme's specificity was 44%, 8.59%, 4.84% and 1.09% better than SVM+existing features, CNN+LBP, CNN and 4D-LBP+WOA-CNN models at 40th training percentage. Thus, the improvement of the suggested WTEEB model was confirmed by these outcomes.

References

1. X. Li *et al.*, Multi-resolution convolutional networks for chest X-ray radiograph based lung nodule detection, *Artificial Intelligence in Medicine*, **23**: 101744, 2020, doi: 10.1016/j.artmed.2019.101744.

2. C.-F.J. Kuo *et al.*, Automatic lung nodule detection system using image processing techniques in computed tomography, *Biomedical Signal Processing and Control*, **56**: 101659, 2020, doi: 10.1016/j.bspc.2019.101659.

3. X. Xu *et al.*, DeepLN: A framework for automatic lung nodule detection using multi-resolution CT screening images, *Knowledge-Based Systems*, **189**: 105128, 2019, doi: 10.1016/j.knosys.2019.105128.

4. Y. Gu *et al.*, Automatic lung nodule detection using a 3D deep convolutional neural network combined with a multi-scale prediction strategy in chest CTs, *Computers in Biology and Medicine*, **103**: 220–231, 2018, doi: 10.1016/j.compbiomed.2018.10.011.

5. Q. Wang, F. Shen, L. Shen, J. Huang, W. Sheng, Lung nodule detection in CT images using a raw patch-based convolutional neural network, *Journal of Digital Imaging,* **32**(6): 971–979, 2019, doi: 10.1007/s10278-019-00221-3.

6. M. Woźniak, D. Połap, G. Capizzi, G. Lo Sciuto, L. Kośmider, K. Frankiewicz, Small lung nodules detection based on local variance analysis and probabilistic neural network, *Computer Methods and Programs in Biomedicine*, **161**: 173–180, 2018, doi: 10.1016/j.cmpb.2018.04.025.

7. W. Zuo, F. Zhou, Z. Li, L. Wang, Multi-resolution CNN and knowledge transfer for candidate classification in lung nodule detection, *IEEE Access*, **7**: 32510–32521, 2019, doi: 10.1109/ACCESS.2019.2903587.

8. H. Jiang, H. Ma, W. Qian, M. Gao Y. Li, An automatic detection system of lung nodule based on multigroup patch-based deep learning network, *IEEE Journal of Biomedical and Health Informatics*, **22**(4): 1227–1237, 2018, doi: 10.1109/JBHI.2017.2725903.

9. E. Toes-Zoutendijk *et al.*, Incidence of interval colorectal cancer after negative results from first-round fecal immunochemical screening tests, by cutoff value and participant sex and age, *Clinical Gastroenterology and Hepatology*, **18**(7): 1493–1500, 2020, doi: 10.1016/j.cgh.2019.08.021.

10. A.J.M. Rombouts, N. Hugen, M.A.G. Elferink, P.M.P. Poortmans, I.D. Nagtegaal, J.H.W. de Wilt, Increased risk for second primary rectal cancer after pelvic radiation therapy, *European Journal of Cancer*, **124**: 142–151, 2020, doi: 10.1016/j.ejca.2019.10.022.

11. Y. Yin *et al.*, Tumor cell load and heterogeneity estimation from diffusion-weighted MRI calibrated with histological data: an example from lung cancer, *IEEE Transactions on Medical Imaging*, **37**(1): 35–46, 2018, doi: 10.1109/TMI.2017.2698525.

12. J. Jiang *et al.*, Multiple resolution residually connected feature streams for automatic lung tumor segmentation from CT images, *IEEE Transactions on Medical Imaging*, **38**(1): 134–144, 2019, doi: 10.1109/TMI.2018.2857800.

13. P. Petousis, A. Winter, W. Speier, D.R. Aberle, W. Hsu, A.A.T. Bui, Using sequential decision making to improve lung cancer screening performance, *IEEE Access*, **7**: 119403–119419, 2019, doi: 10.1109/ACCESS.2019.2935763.

14. S.S. Alahmari, D. Cherezov, D.B. Goldgof, L.O. Hall, R.J. Gillies, M.B. Schabath, Delta radiomics improves pulmonary nodule malignancy prediction in lung cancer screening, *IEEE Access*, **6**: 77796–77806, 2018, doi: 10.1109/ACCESS.2018.28841vif.

15. A. Tremblay *et al.*, Application of lung-screening reporting and data system versus pan-canadian early detection of lung cancer nodule risk calculation in the Alberta lung cancer screening study, *Journal of the American College of Radiology*, **16**(10): 1425–1432, 2019, doi: 10.1016/j.jacr.2019.03.006.

16. Y. Xie, J. Zhang, Y. Xia, Semi-supervised adversarial model for benign–malignant lung nodule classification on chest CT, *Medical Image Analysis*, **57**: 237–248, 2019, doi: 10.1016/j.media.2019.07.004.

17. H. Liu *et al.*, A cascaded dual-pathway residual network for lung nodule segmentation in CT images, *Physica Medica*, **63**: 112–121, 2019, doi: 10.1016/j.ejmp.2019.06.003.

18. V.K. Venugopal *et al.*, Unboxing AI – Radiological insights into a deep neural network for lung nodule characterization, *Academic Radiology*, **27**(1): 88–95, 2020, doi: 10.1016/j.acra.2019.09.015.

19. Y. Nomura *et al.*, Effects of Iierative reconstruction algorithms on computer-assisted detection (CAD) software for lung nodules in ultra-low-dose CT for lung cancer screening, *Academic Radiology*, **24**(2): 124–130, 2017, doi: 10.1016/j.acra.2016.09.023.

20. J. Gong, J.-Y. Liu, L.-J. Wang, B. Zheng, S.-D. Nie, Computer-aided detection of pulmonary nodules using dynamic self-adaptive template matching and a FLDA classifier, *Physica Medica*, **32**(12): 1502–1509, 2016, doi: 10.1016/j.ejmp.2016.11.001.

21. I. Bonavita, X. Rafael-Palou, M. Ceresa, G. Piella, V. Ribas, M.A. González Ballester, Integration of convolutional neural networks for pulmonary nodule malignancy assessment in a lung cancer classification pipeline, *Computer Methods and Programs in Biomedicine*, **185**: 105172, 2020, doi: 10.1016/j.cmpb.2019.105172.

22. N. Tajbakhsh, K. Suzuki, Comparing two classes of end-to-end machine-learning models in lung nodule detection and classification: MTANNs vs. CNNs, *Pattern Recognition*, **63**: 476–486, 2017, doi: 10.1016/j.patcog.2016.09.029.

23. A.A.A. Setio *et al.*, Validation, comparison, and combination of algorithms for automatic detection of pulmonary nodules in computed tomography images: The LUNA16 challenge, *Medical Image Analysis*, **42**: 1–13, 2017, doi: 10.1016/j.media.2017.06.015.

24. M. Toğaçar, B. Ergen, Z. Cömert, Detection of lung cancer on chest CT images using minimum redundancy maximum relevance feature selection method with convolutional neural networks, *Biocybernetics and Biomedical Engineering*, **40**(1): 23–39, 2020, doi: 10.1016/j.bbe.2019.11.004.

25. S.K. Lakshmanaprabu, S.N. Mohanty, K. Shankar, N. Arunkumar, G. Ramirez, Optimal deep learning model for classification of lung cancer on CT images, *Future Generation Computer Systems*, **92**: 374–382, 2019, doi: 10.1016/j.future.2018.10.009.

26. S. Mirjalili, A. Lewis, The whale optimization algorithm, *Advances in Engineering Software*, **95**: 51–67, 2016, doi: 10.1016/j.advengsoft.2016.01.008.

27. J. Yousefi, Image binarization using Otsu thresholding algorithm, 2015, doi: 10.13140/RG.2.1.4758.9284.

28. C.E. Honeycutt, R. Plotnick, Image analysis techniques and gray-level co-occurrence matrices (GLCM) for calculating bioturbation indices and characterizing biogenic sedimentary structures, *Computers & Geosciences*, **34**(11): 1461–1472, 2008, doi: 10.1016/j.cageo.2008.01.006.

29. S. van der Walt *et al.*, scikit-image: image processing in Python, *PeerJ*, **2**: e453, 2014, 10.7717/peerj.453.

30. K. O'Shea, R. Nash, An introduction to convolutional neural networks, *ArXiv e-prints,* arXiv:1511.08458, 10 pages, 2015.

31. M.K. Tripathi, D.D. Maktedar, Optimized deep learning model for mango grading: Hybridizing lion plus firefly algorithm, *IET Image Processing*, **15** (9): 1940–1956, 2021, doi: 10.1049/ipr2.12163.

32. S. Kakad, S. Dhage, Cross domain-based ontology construction via Jaccard Semantic Similarity with hybrid optimization model, *Expert Systems with Applications*, **178**: 115046, 2021, doi: 10.1016/j.eswa.2021.115046.

Received July 30, 2021; revised version November 5, 2021;
accepted November 6, 2021.